

🦉 Otter: Mitigating Background Distractions of Wide-Angle Few-Shot Action Recognition with Enhanced RWKV

Wenbo Huang^{1,2}, Jinghui Zhang^{1*}, Zhenghao Chen³, Guang Li⁴, Lei Zhang^{5*}, Yang Cao², Fang Dong¹, Takahiro Ogawa⁴, Miki Haseyama⁴

¹Southeast University, Nanjing 21189, Jiangsu, China;

²Institute of Science Tokyo, Tokyo 152-8550, Japan;

³The University of Newcastle, Callaghan, NSW 2308, Australia;

⁴Hokkaido University, Sapporo 060-0808, Hokkaido, Japan;

⁵Nanjing Normal University, Nanjing 210023, Jiangsu, China.

wenbohuang1002@outlook.com, {jhzhang, fong}@seu.edu.cn, zhenghao.chen@newcastle.edu.au, {guang, ogawa, mhaseyama}@lmd.ist.hokudai.ac.jp, cao@c.titech.ac.jp, leizhang@njnu.edu.cn

Abstract

Wide-angle videos in few-shot action recognition (FSAR) effectively express actions within specific scenarios. However, without a global understanding of both subjects and background, recognizing actions in such samples remains challenging because of the background distractions. Receptance Weighted Key Value (RWKV), which learns interaction between various dimensions, shows promise for global modeling. While directly applying RWKV to wide-angle FSAR may fail to highlight subjects due to excessive background information. Additionally, temporal relation degraded by frames with similar backgrounds is difficult to reconstruct, further impacting performance. Therefore, we design the **CompOund SegmenTation and Temporal REconstructing RWKV (Otter)**. Specifically, the Compound Segmentation Module (CSM) is devised to segment and emphasize key patches in each frame, effectively highlighting subjects against background information. The Temporal Reconstruction Module (TRM) is incorporated into the temporal-enhanced prototype construction to enable bidirectional scanning, allowing better reconstruct temporal relation. Furthermore, a regular prototype is combined with the temporal-enhanced prototype to simultaneously enhance subject emphasis and temporal modeling, improving wide-angle FSAR performance. Extensive experiments on benchmarks such as SSv2, Kinetics, UCF101, and HMDB51 demonstrate that Otter achieves state-of-the-art performance. Extra evaluation on the VideoBadminton dataset further validates the superiority of Otter in wide-angle FSAR.

Code — <https://github.com/wenbohuang1002/Otter>

1 Introduction

The difficulties of video collection and labeling complicates traditional data-driven training based on fully labeled datasets. Fortunately, few-shot action recognition (FSAR) improves learning efficiency and reduces the labeling dependency by classifying unseen actions from extremely few

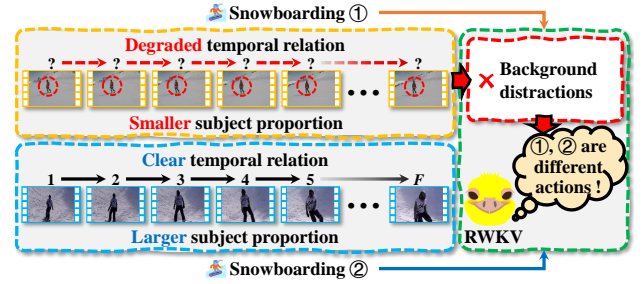


Figure 1: Smaller subject proportion (red circles) and degraded temporal relation (red dotted lines) both contribute to background distractions in wide-angle FSAR. As a result, wide-angle samples are more challenging to recognize compared with regular samples.

video samples. Therefore, FSAR has diverse real-world applications, including health monitoring and motion analysis (Yan et al. 2023; Wang et al. 2023b). However, recognizing similar actions under regular viewpoint is a non-trivial problem in FSAR. For instance, distinguishing “indoor climbing” and “construction working” is challenging, as subjects exhibit similar actions against a wall. To mitigate this issue, wide-angle videos provide contextual background, such as a “climbing wall” or a “construction site”, expressing actions within specific scenarios more accurately. According to established definitions (Lai et al. 2021; Zhang et al. 2025), wide-angle videos with a greater field of view (FoV) are widespread*. FoV estimation (Lee et al. 2021; Hold-Geoffroy et al. 2023) on popular FSAR benchmarks further reveals that approximately 35% of samples per dataset fall into this category, yet remain unexplored.

On the other hand, effectively modeling wide-angle videos remains a critical issue due to the difficulty of accurately interpreting both subjects and background content. Recent success in recurrent model-based architectures

*Corresponding author.

*This work adopts the widely accepted definition of wide-angle as FoV exceeding 80°.

has led to methods such as Receptance Weighted Key Value (RWKV) (Peng et al. 2023, 2024), which demonstrate strong performance in global modeling across various tasks by enabling token interaction through linear interpolation, thereby expanding the receptive field and efficiently capturing subject-background dependencies.

To seamlessly apply RWKV in wide-angle FSAR, two key challenges remain, primarily due to background distractions, as illustrated in Figure 1. *Challenge 1: Lack of primary subject highlighting in RWKV.* As shown in the “snowboarding” examples, the primary subject occupies a smaller proportion in wide-angle frames. When RWKV is directly applied for global feature extraction, it tends to capture massive secondary background information “snow” rather than the primary subject “athlete”. Since the background serves as contextual information while the subject is crucial for determining feature representation, this reversal of primary and secondary information may lead to potential misclassification. *Challenge 2: Absence of temporal relation reconstruction in RWKV.* Temporal relation plays a significant role in FSAR, primarily in perceiving action direction and aligning frames. From the “snowboarding” example, we observe that abundant background information in similar frames obscures the evolution of primary subject “athlete”, causing temporal relation degraded in wide-angle samples. However, RWKV focuses on global modeling but lacks the capability to reconstruct temporal relation, increasing the difficulty of recognizing wide-angle samples.

Although current attempts achieve promising results (Fu et al. 2020; Wang et al. 2023a; Perrett et al. 2021; Huang et al. 2024; Wang et al. 2022; Xing et al. 2023a), few works address the two aforementioned challenges simultaneously. Therefore, we propose the **Compound Segmentation and Temporal REconstructing RWKV (Otter)**, which highlights subjects and restores temporal relations in wide-angle FSAR. To be specific, we devise the Compound Segmentation Module (CSM) to adaptively segment each frame into patches and highlight the subject before feature extraction. This enables RWKV to focus on the subject rather than being overwhelmed by secondary background information. We further design the Temporal Reconstruction Module (TRM), integrated into temporal-enhanced prototype construction to perform bidirectional feature scanning across frames, enabling RWKV to reconstruct temporal relations degraded in wide-angle videos. Additionally, we combine a regular prototype with a temporal-enhanced prototype to simultaneously achieve subject highlighting and temporal relation reconstruction. This strategy significantly improves the performance of wide-angle FSAR.

To the best of our knowledge, the proposed Otter is the first attempt of utilizing RWKV for wide-angle FSAR. The core contribution is threefold.

- The CSM is introduced to highlight the primary subject in RWKV. It segments each frame into multiple patches, learns adaptive weights from each patch to highlight the subject, and then reassembles the patches in their original positions. This process enables more effective detection of inconspicuous subjects in wide-angle FSAR.

- The TRM is designed to reconstruct temporal relations in RWKV. It performs bidirectional scanning of frame features and reconstructs the temporal relation via a weighted average of the scanning results for the temporal-enhanced prototype. This module mitigates temporal relation degradation in wide-angle FSAR.
- The state-of-the-art (SOTA) performance achieved by Otter is validated through extensive experiments on prominent FSAR benchmarks, including SSv2, Kinetics, UCF101, and HMDB51. Additional analyses on wide-angle VideoBadminton dataset emphasize superiority of Otter, particularly in wide-angle FSAR.

2 Related works

2.1 Few-Shot Learning

Few-shot learning, which aims to classify unseen classes using extremely limited samples, is a crucial area in the deep learning community (Fei-Fei, Fergus, and Perona 2006). It encompasses three main paradigms: augmentation, optimization, and metric-based. Augmentation-based methods (Hariharan and Girshick 2017; Wang et al. 2018; Zhang et al. 2018; Chen et al. 2019; Li et al. 2020) address data scarcity by generating synthetic samples to augment the training set. In contrast, optimization-based methods (Finn, Abbeel, and Levine 2017; Ravi and Larochelle 2017; Rusu et al. 2018; Jamal and Qi 2019; Rajeswaran et al. 2019) focus on modifying the optimization process to enable efficient fine-tuning with few samples. Among these approaches, the metric-based paradigm (Snell, Swersky, and Zemel 2017; Oreshkin, Rodríguez López, and Lacoste 2018; Sung et al. 2018; Hao et al. 2019; Wang et al. 2020) is the most widely adopted in practical applications due to its simplicity and effectiveness. Specifically, these methods construct class prototypes and perform classification by the similarity between query features and class prototypes using learnable metrics.

2.2 Few-Shot Action Recognition

Metric-based meta-learning is the mainstream paradigm in FSAR due to its simplicity and effectiveness. This approach embeds support features into class prototypes to represent various classes. Most methods rely on temporal alignment to match queries with prototypes. For example, the dynamic time warping (DTW) algorithm is used in OTAM for similarity calculation (Cao et al. 2020). Subsequent works, including ITANet (Zhang, Zhou, and He 2021), T²AN (Li et al. 2022), and STRM (Thatipelli et al. 2022), further optimize temporal alignment. To focus more on local features, TRX (Perrett et al. 2021), HyRSM (Wang et al. 2022), SloshNet (Xing et al. 2023b), SA-CT (Zhang et al. 2023), and Manta (Huang et al. 2025) employ fine-grained or multi-scale modeling. Additionally, models are enhanced with supplementary information such as depth (Fu et al. 2020), optical flow (Wanyan et al. 2023), and motion cues (Wang et al. 2023a; Wu et al. 2022; Huang et al. 2024). Despite achieving satisfactory performance, They are unable to address challenges in wide-angle FSAR simultaneously.

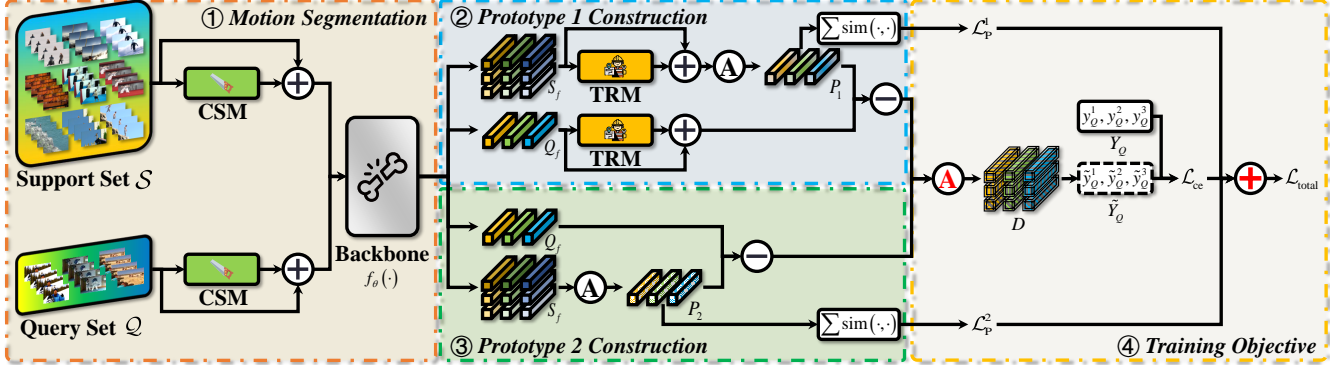


Figure 2: The overall architecture of the Otter. Main components CSM and TRM are specified combination of core units (§ 3.3). To be specific, ① Motion Segmentation with CSM and backbone (§ 3.4). ② Prototype 1 Construction with TRM for reconstructing temporal relation (§ 3.5). ③ Prototype 2 Construction with regular prototype (§ 3.5). ④ Training Objective $\mathcal{L}_{\text{total}}$ is the loss combination of cross-entropy loss \mathcal{L}_{ce} , \mathcal{L}_p^1 from ②, and \mathcal{L}_p^2 from ③ (§ 3.6). Notion $\textcircled{A}/\textcircled{A}$: averaging/weighted averaging. $\textcircled{+}/\textcircled{+}$: element-wise plus/weighted element-wise plus.

2.3 RWKV Model

The RWKV model is initially proposed for natural language processing (NLP) (Peng et al. 2023, 2024), combining the parallel processing capabilities of Transformers with the linear complexity of RNNs. This fusion enables RWKV to achieve efficient global modeling with reduced memory usage and accelerated inference speed following data-driven training. Building on this foundation, the vision-RWKV (VRWKV) model is developed for computer vision tasks and has demonstrated notable success (Duan et al. 2024). Additionally, numerous studies have explored integrating RWKV with Diffusion or CLIP, achieving remarkable results in various domains (Fei et al. 2024; Gu et al. 2024; He et al. 2024; Yuan et al. 2024). However, the potential of RWKV in wide-angle FSAR remains unexplored.

3 Methodology

3.1 Problem Definition

Following settings in previous literature (Cao et al. 2020; Perrett et al. 2021), three parts including training set $\mathcal{D}_{\text{train}}$, validation set \mathcal{D}_{val} , and testing set $\mathcal{D}_{\text{test}}$ without overlap ($\mathcal{D}_{\text{train}} \cap \mathcal{D}_{\text{val}} \cap \mathcal{D}_{\text{test}} = \emptyset$) are divided from datasets. Each part is further split into two non-overlapping sets including support \mathcal{S} with at least one labeled sample of each class and query \mathcal{Q} with all unlabeled samples ($\mathcal{S} \cap \mathcal{Q} = \emptyset$). The aim of FSAR is to classify samples from \mathcal{Q} into one class of \mathcal{S} . A large number of few-shot tasks are randomly selected and combined from $\mathcal{D}_{\text{train}}$. We define few-shot setting as N -way K -shot from \mathcal{S} with N classes, K samples in each class.

Successive F frames are uniformly extracted from a video each time. The k^{th} ($k = 1, \dots, K$) sample of the n^{th} ($n = 1, \dots, N$) class of \mathcal{S} is defined as $S^{n,k}$ and randomly selected sample from \mathcal{Q} is denoted as Q^r ($r \in \mathbb{Z}^+$).

$$\begin{aligned} S^{n,k} &= [s_1^{n,k}, \dots, s_F^{n,k}] \in \mathbb{R}^{F \times C \times H \times W}, \\ Q^r &= [q_1^r, \dots, q_F^r] \in \mathbb{R}^{F \times C \times H \times W}, \end{aligned} \quad (1)$$

in which F , C , H , and W represent frames, channels, height, and width, respectively.

3.2 Overall Architecture

We demonstrate the overall architecture of Otter via a simple 3-way 3-shot example in Figure 2. The following two main components of Otter are built from specific combinations of core units (§ 3.3). At the first stage of motion segmentation, CSM works for highlighting subjects before feature extracting via backbone (§ 3.4). TRM is introduced in the second stage of prototype 1 (temporal-enhanced) construction, reconstructing the temporal relation (§ 3.5). Prototype 2 (regular) construction is the third stage, retaining subject emphasis (§ 3.5). Finally, distances calculated from weighted average of two prototypes are employed in cross-entropy loss \mathcal{L}_{ce} . In order to further distinguish class prototypes, the prototype similarities serve as \mathcal{L}_p^1 and \mathcal{L}_p^2 . The weighted combination of three loss including \mathcal{L}_{ce} , \mathcal{L}_p^1 and \mathcal{L}_p^2 is the training objective $\mathcal{L}_{\text{total}}$ (§ 3.6).

3.3 Core Units

In order to simplify equation writing, we use wildcard symbol Δ . Self-attention can be simulated through five tensors: receptance R , weight W , key K^* , value V , and gate G . To handle spatial, temporal, and channel-wise features, we design three core units: Spatial Mixing, Temporal Mixing, and Channel Mixing, inspired by the architecture of RWKV-5/6. The main components, CSM and TRM, are specific combinations of these core units, for subject highlighting and temporal relation reconstruction in wide-angle FSAR.

To be specific, Spatial Mixing (Figure 3a) is designed to aggregate features from different spatial locations. Let r_t , k_t , v_t , and g_t denote the t^{th} features of R , K^* , V , and G , respectively. This design allows the model to capture dependencies across different regions of the image, thereby enhancing its

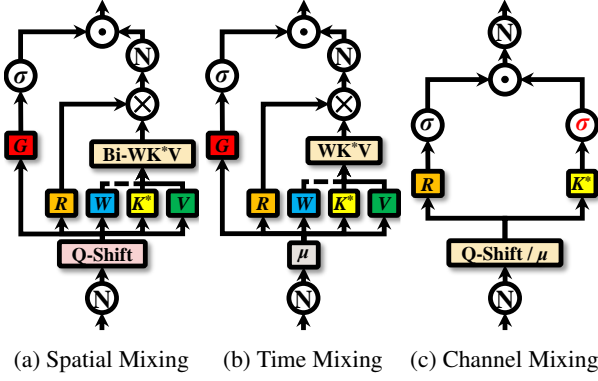


Figure 3: Core units of RWKV. \textcircled{N} : normalization, \otimes/\oslash : matrix/element-wise multiplication, \odot : activation function.

ability to model global spatial features.

$$\begin{aligned}\Delta_t &= W_\Delta \cdot \text{Q-Shift}_\Delta(x) \\ &= W_\Delta \cdot [x + (1 - \mu_\Delta) \odot x'], \forall \Delta \in \{r, k^*, v, g\}, \\ x'_{[h', w']} &= \text{Concat}(x_{[h'-1, w', 0: C/4]}, x_{[h'+1, w', C/4: C/2]}, \\ &\quad x_{[h', w'-1, C/2: 3C/4]}, x_{[h', w'+1, 3C/4: C]}),\end{aligned}\quad (2)$$

where μ is a learnable vector for the calculation of R, K^* , and V while $\text{Concat}(\cdot)$ means concatenate operation. “ \cdot ” separates the start and end index. Row and column index of x are denoted by h' and w' . Then attention result $(wk^*v)_t$ is calculated according to the following definition.

$$\begin{aligned}(wk^*v)_t &= \text{Bi-WK}^*V(K^*, V)_t \\ &= \frac{\sum_{i=0, i \neq t}^{t-1} e^{-(|t-i|-1) \cdot w + k_i^*} v_i + e^{u + k_t^*} v_t}{\sum_{i=0, i \neq t}^{t-1} e^{-(|t-i|-1) \cdot w + k_i^*} + e^{u + k_t^*}},\end{aligned}\quad (3)$$

W is determined by vector w . After combining with r_t and g_t , the o^{th} feature of output O can be calculated as

$$o_t = \sigma(g_t) \odot \text{Norm}(r_t \otimes (wk^*v)_t), \quad (4)$$

in which $\sigma(\cdot)$ denotes activation function while $\text{Norm}(\cdot)$ represents normalization.

As illustrated Figure 3b, we observe that the main discrepancies between Time Mixing and Spatial Mixing are Δ_t and $\text{WK}^*V(\cdot)$. The former one can be defined as

$$\Delta_t = W_\Delta \cdot [x_t + (1 - \mu_\Delta) \odot x_t - 1], \forall \Delta \in \{r, k^*, v, g\}, \quad (5)$$

while the latter can be written as

$$\begin{aligned}(wk^*v)_t &= \text{WK}^*V(K^*, V)_t \\ &= \frac{\sum_{i=0, i \neq t}^{t-1} e^{-(t-i-1) \cdot w + k_i^*} v_i + e^{u + k_t^*} v_t}{\sum_{i=0, i \neq t}^{t-1} e^{-(t-i-1) \cdot w + k_i^*} + e^{u + k_t^*}},\end{aligned}\quad (6)$$

After achieving O with the same way, the combination of current and past states enable long-term modeling.

In order to capture dependencies between multiple dimensions of input, Channel Mixing (Figure 3c) mixes information from various channels by R and V , as

$$O = \sigma_r(R) \odot \sigma_v(V). \quad (7)$$

$\sigma_r(\cdot)$ and $\sigma_v(\cdot)$ means two difference kinds of activation function applied for R and V .

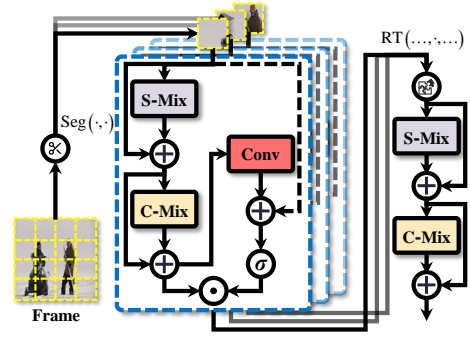


Figure 4: The structure of Compound Segmentation Module (CSM).

3.4 Motion Segmentation

Compound Segmentation Module (CSM) As demonstrated in Figure 4, each frame is segmented into HW/p^2 patches with $\text{Seg}(\cdot, \cdot)$. Using random frames $s, q \in \mathbb{R}^{C \times H \times W}$ from $S^{n,k}, Q^r$ as simple examples.

$$\Delta^p = \text{Seg}(\Delta, p) \in \mathbb{R}^{C \times p \times p}, \forall \Delta \in \{s, q\}. \quad (8)$$

H and W must be divisible by p . The operations of Spatial Mixing, Time Mixing, and Channel Mixing can be written as $\text{S-Mix}(\cdot)$, $\text{T-Mix}(\cdot)$, and $\text{C-Mix}(\cdot)$, respectively. The output Δ^α of $\text{S-Mix}(\cdot)$ is connected with the input Δ^p for capturing region associations of patches, as

$$\Delta^\alpha = [\text{S-Mix}(\Delta^p) \oplus \Delta^p] \in \mathbb{R}^{C \times p \times p}, \forall \Delta \in \{s, q\}. \quad (9)$$

The activation function $\sigma(\cdot)$ in $\text{S-Mix}(\cdot)$ is Sigmoid(\cdot). Through the same method of connection with Δ^α , the output Δ^β of $\text{T-Mix}(\cdot)$ can be achieved.

$$\Delta^\beta = [\text{C-Mix}(\Delta^\alpha) \oplus \Delta^\alpha] \in \mathbb{R}^{C \times p \times p}, \forall \Delta \in \{s, q\}, \quad (10)$$

where the $\sigma_r(\cdot)$ and $\sigma_v(\cdot)$ of $\text{C-Mix}(\cdot)$ are Sigmoid(\cdot) and Relu(\cdot). Following C3-STISR (Zhao et al. 2022), learnable weights $lw^\Delta \in \mathbb{R}^{C \times p \times p}$ can be achieved from Δ^p and Δ^β via convolution $\text{Conv}(\cdot)$ and residual connection.

$$lw^\Delta = \text{Sigmoid}[\text{Conv}(\Delta^\beta) \oplus \Delta^p], \forall \Delta \in \{s, q\}. \quad (11)$$

Restoring all element-wise multiplication of lw^Δ and Δ^β can highlight subject in frames. We write the corresponding operation in $\text{RT}(\cdot, \cdot, \cdot)$ with the output $\hat{\Delta}$.

$$\hat{\Delta} = \text{RT}(\cdot, lw^\Delta \odot \Delta^\beta, \cdot) \in \mathbb{R}^{C \times H \times W}, \forall \Delta \in \{s, q\}. \quad (12)$$

According to (9) and (10), the final outputs $\hat{\Delta}(\forall \Delta \in \{s, q\})$ of CSM are calculated via $\text{S-Mix}(\cdot)$ and $\text{C-Mix}(\cdot)$. We place each $\hat{\Delta}$ in its raw position for residual connection with inputs $\hat{S}^{n,k}, \hat{Q}^\gamma$, thereby achieving subject highlighting.

Feature Extraction D -dimensional features $S_f^{n,k}, Q_f^\gamma \in \mathbb{R}^{F \times D}$ are extracted by sending $\hat{S}^{n,k}, \hat{Q}^\gamma$ into backbone $f_\theta(\cdot): \mathbb{R}^{C \times H \times W} \mapsto \mathbb{R}^D$.

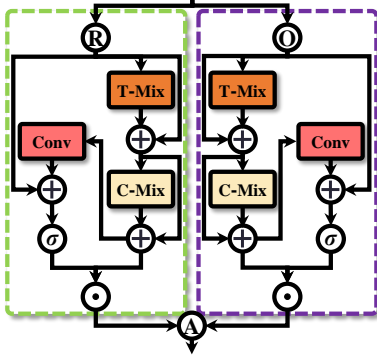


Figure 5: The structure of Temporal Reconstruction Module (TRM). \odot : ordered scanning. \circledast : reserved scanning.

3.5 Prototype Construction

Temporal Reconstruction Module (TRM) In order to reconstruct temporal relation, TRM illustrated in Figure 5 has two branches for bidirectional scanning of $S_f^{n,k}$ and Q_f^γ . Using ordered Δ as an example, T-Mix (\cdot) with SiLU (\cdot) and C-Mix (\cdot) are applied based on (9) and (10) for long-term modeling. Learned weight lw^Δ can also be achieved according to (11). The ordered output Δ is the element-wise multiplication of lw^Δ and Δ :

$$\Delta = [lw^\Delta \odot \Delta] \in \mathbb{R}^{F \times D}, \forall \Delta \in \{S_f^{n,k}, Q_f^\gamma\}. \quad (13)$$

In the same way, reversed output $\hat{\Delta}$ can also be achieved. The final result $\tilde{\Delta}$ is the average Avg (\cdot, \cdot) of Δ and $\hat{\Delta}$ connected with the original input, as:

$$\tilde{\Delta} = [\Delta + \text{Avg}(\Delta, \hat{\Delta})] \in \mathbb{R}^{F \times D}, \forall \Delta \in \{S_f^{n,k}, Q_f^\gamma\}. \quad (14)$$

After the TRM, temporal relation is recovered.

Prototype and Distance P_1^n is prototype of the n^{th} support class, being achieved via average calculation of $\tilde{S}_f^{n,k}$:

$$P_1^n = \frac{1}{K} \sum_{k=1}^K \tilde{S}_f^{n,k} \in \mathbb{R}^{F \times D}. \quad (15)$$

The distance between \tilde{Q}_f^γ and P_1^n is D_1 .

$$D_1 = \|P_1^n - \tilde{Q}_f^\gamma\|. \quad (16)$$

For further distinguishing classes of the prototype P_1 , we apply the sum of cosine similarity function Sim (\cdot, \cdot) for \mathcal{L}_P^1 :

$$\mathcal{L}_P^1 = \sum_{n \neq n'} \text{Sim}(P_1^n, P_1^{n'}), (P_1^n, P_1^{n'}) \in P_1. \quad (17)$$

The prototype 2 is constructed without TRM. Therefore, the n^{th} support prototype P_2^n can be computed from $S_f^{n,k}$. Then the corresponding distance D_2 between Q_f^γ and P_2^n can also be achieved. After the same cosine similarity calculation, \mathcal{L}_P^2 is applied for differentiating classes of P_2 .

3.6 Training Objective

The distance D between n^{th} class and Q_f^γ is the weighted mean value of D_1 and D_2 with weight ω . Therefore, the predicted label $\tilde{y}_Q^j \in \tilde{Y}_Q$ of query is

$$\tilde{y}_Q^j = \underset{n}{\text{argmin}}(D), D = \sum_{i=1}^2 \omega_i D_i. \quad (18)$$

\tilde{y}_Q^j and the ground truth $y_Q^j \in Y_Q$ are applied in cross-entropy loss \mathcal{L}_{ce} calculation.

$$\mathcal{L}_{ce} = -\frac{1}{N} \sum_{j=1}^N y_Q^j \log(\tilde{y}_Q^j). \quad (19)$$

The training objective $\mathcal{L}_{\text{total}}$ is the combination of \mathcal{L}_{ce} , \mathcal{L}_P^1 , and \mathcal{L}_P^2 under weight factor λ as:

$$\mathcal{L}_{\text{total}} = \lambda_0 \mathcal{L}_{ce} + \lambda_1 \mathcal{L}_P^1 + \lambda_2 \mathcal{L}_P^2, \quad (20)$$

4 Experiments

4.1 Experimental Configuration

Data Processing Temporal-related SSv2 (Goyal et al. 2017), spatial-related Kinetics (Carreira and Zisserman 2017), UCF101 (Kay et al. 2017), and HMDB51 (Kuehne et al. 2011) are most frequently-used benchmark datasets for FSAR. A wide-angle dataset VideoBadminton (Li et al. 2024) is employed for evaluating real-world performance. In order to prove the effectiveness of our Otter, the sampling intervals setting of decoding videos are each 1 frame. Based on widely-used data split (Zhu and Yang 2018; Cao et al. 2020; Zhang et al. 2020), $\mathcal{D}_{\text{train}}$, \mathcal{D}_{val} , and $\mathcal{D}_{\text{test}}$ ($\mathcal{D}_{\text{train}} \cap \mathcal{D}_{\text{val}} \cap \mathcal{D}_{\text{test}} = \emptyset$) are divided from each dataset. Then further split of support \mathcal{S} and query \mathcal{Q} are executed for FSAR.

According to TSN (Wang et al. 2016), each frame are sized into $3 \times 256 \times 256$ while F of successive frames is set to 8. $3 \times 224 \times 224$ random crops and horizontal flipping data augmentation is applied during training while only the center crop is utilized in testing. As an exception, horizontal flipping is absent in SSv2 because of many actions with horizontal direction such as “Pulling S from left to right”[†].

Implementation Details and Evaluation Metrics Standard 5-way 1-shot and 5-shot setting are adopted for FSAR. We select ResNet-50, ViT-B, VMamba-B, and VRWKV-B with ImageNet pre-trained weights initialization as our backbone. The dimension D of features is 2048.

The larger SSv2 are trained with 75,000 tasks while other datasets only require 10,000 tasks. SGD optimization for training is applied with initial learning rate 10^{-3} . The \mathcal{D}_{val} determines hyper-parameters such as distance weight ($\omega_1 = \omega_2 = 0.5$), weight factor of loss λ ($\lambda_0 = 0.8, \lambda_1 = \lambda_2 = 0.1$) and patch size ($p = 56$). Average accuracy of 10,000 random tasks from $\mathcal{D}_{\text{test}}$ is recorded during testing stage. Experiments are most conducted on a server with two 32GB NVIDIA Tesla V100 PCIe GPUs.

[†]“S” means “something”.

Methods	Reference	Pre-Backbone	SSv2		Kinetics		UCF101		HMDB51	
			1-shot	5-shot	1-shot	5-shot	1-shot	5-shot	1-shot	5-shot
STRM (Thatipelli et al. 2022)	CVPR'22	ImageNet-RN50	N/A	68.1	N/A	86.7	N/A	96.9	N/A	76.3
SloshNet (Xing et al. 2023a)	AAAI'23	ImageNet-RN50	46.5	68.3	N/A	87.0	N/A	97.1	N/A	77.5
SA-CT (Zhang et al. 2023)	MM'23	ImageNet-RN50	48.9	69.1	71.9	87.1	85.4	96.3	61.2	76.9
GCSM (Yu et al. 2023)	MM'23	ImageNet-RN50	N/A	N/A	74.2	88.2	86.5	97.1	61.3	79.3
GgHM (Xing et al. 2023b)	ICCV'23	ImageNet-RN50	54.5	69.2	74.9	87.4	85.2	96.3	61.2	76.9
STRM (Thatipelli et al. 2022)	CVPR'22	ImageNet-ViT	N/A	70.2	N/A	91.2	N/A	98.1	N/A	81.3
SA-CT (Zhang et al. 2023)	MM'23	ImageNet-ViT	N/A	66.3	N/A	91.2	N/A	98.0	N/A	81.6
*TRX (Perrett et al. 2021)	CVPR'21	ImageNet-RN50	53.8	68.8	74.9	85.9	85.7	96.3	83.5	85.5
*HyRSM (Wang et al. 2022)	CVPR'22	ImageNet-RN50	54.1	68.7	73.5	86.2	83.6	94.6	80.2	86.1
*MoLo (Wang et al. 2023a)	CVPR'23	ImageNet-RN50	56.6	70.7	74.2	85.7	86.2	95.4	87.3	86.3
*SOAP (Huang et al. 2024)	MM'24	ImageNet-RN50	61.9	85.8	86.1	93.8	94.1	<u>99.3</u>	86.4	88.4
*Manta (Huang et al. 2025)	AAAI'25	ImageNet-RN50	<u>63.4</u>	<u>87.4</u>	<u>87.4</u>	<u>94.2</u>	<u>95.9</u>	<u>99.2</u>	<u>86.8</u>	<u>88.6</u>
*MoLo (Wang et al. 2023a)	CVPR'23	ImageNet-ViT	61.1	71.7	78.9	95.8	88.4	97.6	81.3	84.4
*SOAP (Huang et al. 2024)	MM'24	ImageNet-ViT	<u>66.7</u>	87.2	<u>89.9</u>	95.5	96.8	<u>99.5</u>	<u>89.3</u>	<u>89.8</u>
*Manta (Huang et al. 2025)	AAAI'25	ImageNet-ViT	66.2	<u>89.3</u>	88.2	<u>96.3</u>	<u>97.2</u>	<u>99.5</u>	88.9	88.8
*MoLo (Wang et al. 2023a)	CVPR'23	ImageNet-ViR	60.9	71.8	79.1	95.7	88.2	97.5	81.2	84.6
*SOAP (Huang et al. 2024)	MM'24	ImageNet-ViR	66.4	87.1	<u>89.8</u>	95.8	96.6	99.1	<u>88.8</u>	<u>89.7</u>
*Manta (Huang et al. 2025)	AAAI'25	ImageNet-ViR	<u>66.5</u>	<u>89.2</u>	88.1	<u>96.1</u>	<u>96.7</u>	<u>99.2</u>	<u>88.7</u>	<u>89.5</u>
AmeFu-Net (Fu et al. 2020)	MM'20	ImageNet-RN50	N/A	N/A	74.1	86.8	85.1	95.5	60.2	75.5
MTFAN (Wu et al. 2022)	CVPR'22	ImageNet-RN50	45.7	60.4	74.6	87.4	84.8	95.1	59.0	74.6
AMFAR (Wanyan et al. 2023)	CVPR'23	ImageNet-RN50	61.7	79.5	80.1	92.6	91.2	99.0	73.9	87.8
*Lite-MKD (Liu et al. 2023)	MM'23	ImageNet-RN50	55.7	69.9	75.0	87.5	85.3	96.8	66.9	74.7
*Lite-MKD (Liu et al. 2023)	MM'23	ImageNet-ViT	59.1	73.6	78.8	90.6	89.6	98.4	71.1	77.4
*Lite-MKD (Liu et al. 2023)	MM'23	ImageNet-ViR	59.1	73.7	78.5	90.5	89.7	97.9	71.2	77.5
Otter	Ours	ImageNet-RN50	64.7	88.5	90.5	96.4	96.8	99.2	88.1	89.8
Otter	Ours	ImageNet-ViT	67.2	89.9	91.8	97.3	97.7	99.4	89.9	90.6
Otter	Ours	ImageNet-ViR	67.1	89.8	91.7	96.8	97.5	99.3	89.5	90.5

Table 1: Comparison (\uparrow Acc. %) on ResNet-50 (ImageNet-RN50), ViT-B (ImageNet-ViT), and VRWKV-B (ImageNet-ViR) are separated by dashed line. **Bold texts** denotes the global best results while Underline texts serve as the local best. From top to bottom, the whole table is divided into three parts including RGB-based, multimodal, and our Otter. In the first two parts, “*” represents our implementation with the same setting. “N/A” indicates not available.

4.2 Comparison with Various Methods

We implement many methods under the same setting for fair comparison with Otter. The average accuracy (\uparrow higher indicates better) is illustrated in Table 1.

ResNet-50 Methods Using SSv2 under 1-shot setting as representative results, we find that Otter outperforms the current SOTA method Manta which focuses on long subsequences from 63.4% to 64.7%. A similar improvement can also be discovered in other datasets with different shots.

ViT-B Methods The larger model capacity makes ViT-B perform better than ResNet-50. We observe that the previous SOTA performance is achieved by SOAP or Manta. Being similar with ResNet-50, Otter reveals superior performance, surpassing previous methods.

VRWKV-B Methods As an emerging model, VRWKV-B can efficiently extract feature from promising regions association. Compared with other backbones, we observe that the overall trend in performance has no significant changes. The proposed Otter focus on improving wide-angle samples, achieving new SOTA performance.

4.3 Essential Components and Factors

Key Components In order to analyze the effect of key components in Otter, we conduct experiments with only

CSM	TRM	SSv2		Kinetics	
		1-shot	5-shot	1-shot	5-shot
\times	\times	54.6	69.2	78.1	85.3
\checkmark	\times	61.3	85.6	89.4	94.8
\times	\checkmark	59.5	83.4	87.8	92.7
\checkmark	\checkmark	64.7	88.5	90.5	96.4

Table 2: Comparison (\uparrow Acc. %) of key components.

CSM, TRM, and both of them. As demonstrated in Table 2, we observe that CSM and TRM both improve the performance. In our design, CSM highlights subject within wide-angle frames before feature extraction. Then TRM reconstructs the degraded temporal relations. Two modules operate successively and complement each other, indicating that full Otter achieves optimal performance.

Patch Design in CSM A deeper research on patch design in CSM is indicated in Table 3. It is obvious that the performance is increasing with more fine grained design segmentation (less p). If p is further reduced to 28, the performance will have a decline. We also consider multi-scale patch configurations and observe that $p=56$ consistently performs better. This may be attributed to the fact that multi-scale design introduces redundant features. Therefore, we adopt $p=56$

p	SSv2		Kinetics	
	1-shot	5-shot	1-shot	5-shot
$p = 224$	62.7	86.4	87.7	94.6
$p = 112$	63.6	87.1	89.5	95.2
$p = 56$	64.7	88.5	90.5	96.4
$p = 28$	64.1	87.9	90.2	95.8
$p \in \{28, 56\}$	64.2	88.1	90.1	96.1
$p \in \{56, 112\}$	63.7	87.9	89.6	95.8

Table 3: Comparison (\uparrow Acc. %) of patch design in CSM.

⓪	Ⓜ	SSv2		Kinetics	
		1-shot	5-shot	1-shot	5-shot
✓	✗	63.2	87.3	89.7	95.7
✗	✓	60.6	85.2	89.1	94.2
✓	✓	64.7	88.5	90.5	96.4

Table 4: Comparison (\uparrow Acc. %) of direction design in TRM.

with 4×4 segmentation in our patch design.

Direction Design in TRM As illustrated in Table 4, the experiments with unidirectional and bidirectional scanning is conducted to verify the effect of direction design in TRM. Two types of unidirectional scanning are inferior to bidirectional design. The reserved scanning (Ⓜ) even harms the performance of ordered scanning (⓪). This may be explained by the confusion of directional related actions. Therefore, the bidirectional design is indispensable in TRM.

4.4 Wide-Angle Evaluation

Performance on Wide-Angle Dataset In order to evaluate Otter on wide-angle scenario, we employ VideoBadminton dataset with all wide-sample samples for testing. Form the results in Table 5, it is Otter that obviously far ahead of other methods without specific design for wide-angle samples. Owing to highlighted subject and reconstructed temporal relation, Otter mitigates background distractions. Therefore, the performance on challenging wide-angle samples is significantly improved.

Methods	VB→VB		KI→VB	
	1-shot	5-shot	1-shot	5-shot
MoLo	60.2	64.5	58.9	61.7
SOAP	63.5	66.9	60.1	63.1
Manta	64.1	67.1	62.1	65.3
Otter	71.2	75.8	69.5	72.6

Table 5: Comparison (\uparrow Acc. %) with wide-angle dataset. VB→VB: training and testing both on VideoBadminton, KI→VB: Kinetics training while VideoBadminton testing.

CAM Visualization In Figure 6, subjects are inconspicuous and similar background makes temporal relation degradation. From the CAM results without Otter, the focuses of model are mostly in the background while the subject in distance is entirely ignored. When being equipped with Otter, most of focuses are transferred to subjects and background is

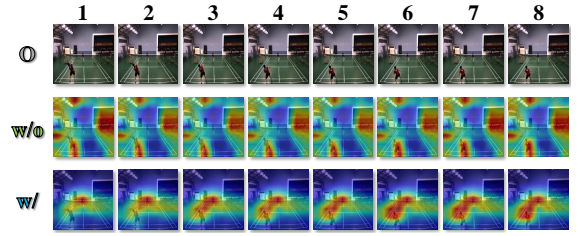


Figure 6: CAM of “smash” from VideoBadminton. O: Original, w/: with Otter, w/o: without Otter.

not completely overlooked. Compared with only focusing on the subject nearby, Otter can capture both of subjects playing badminton. These prove that Otter helps the model better understand “smash”, an action that requires interaction between two subjects, mitigating background distractions and achieving better performance in wide-angle FSAR.

Various FoV To rigorously evaluate Otter on wide-angle samples, frames with varying FoV are essential. Given that FoV is primarily determined by complementary metal oxide semiconductor (CMOS) size and lens focal length (Liao et al. 2023), we utilized PQDiff (Zhang et al. 2024) for out-painting magnification (U_m) and introduced the distortion factor (U_d) in the VideoBadminton dataset to simulate diverse CMOS sizes and focal lengths. This approach results in five distinct FoV levels, with higher levels indicating a wider FoV. As indicated in Figure 7, we observe that recent methods all have a drastic downward trend with the increasing level of FoV. Although our Otter is also negatively influenced, the downward trend is much more stable, revealing the outstanding performance of wide-angle FSAR.

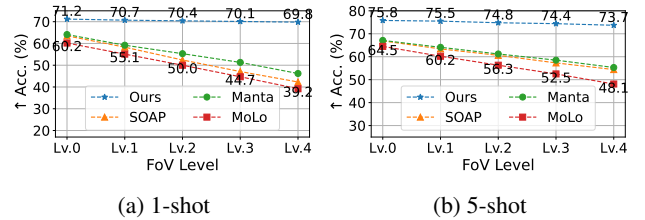


Figure 7: Comparison (\uparrow Acc. %) with various FoV levels.

5 Conclusion

In this work, we propose Otter which is specially designed against background distractions of wide-angle FSAR. Otter highlights subjects in each frames via adaptive segmentation and enhancement of CSM. Temporal relation degradation caused by too many frames with similar background is reconstructed by bidirectional scanning of TRM. Otter achieves new SOTA performance on several widely-used datasets. Further studies demonstrate the competitiveness of our proposed method, especially for mitigating background distractions of wide-angle FSAR. We hope this work will inspire upcoming research in FSAR community.

Supplementary Materials

In the supplementary material, we provide:

- Extra Study of Key Components (mentioned in § 4.3)
- Additional Wide-Angle Evaluation (mentioned in § 4.4)
- Robustness Study
- Computational Complexity

A Extra Study of Key Components

A.1 Study on RWKV-4 and RWKV-5/6

Currently, RWKV-4 (Peng et al. 2023) and RWKV-5/6 (Peng et al. 2024) are released official versions. The main discrepancy is additional gate G mechanism in RWKV-5/6 for the control of information flow. In order to compare the performance, we conduct experiments with three key components under various basis. The results are demonstrated in Table I. We find that applying RWKV-5/6 performs better than components based on RWKV-4. Therefore, we select the updated RWKV-5/6 as the basis of our proposed Otter.

S-Mix	T-Mix	C-Mix	SSv2		Kinetics	
			1-shot	5-shot	1-shot	5-shot
R-4	R-4	R-4	64.0	87.5	89.2	94.3
R-5/6	R-4	R-4	64.2	87.4	89.5	94.5
R-4	R-5/6	R-4	64.1	87.6	89.1	94.7
R-4	R-4	R-5/6	64.0	87.4	89.4	94.4
R-5/6	R-5/6	R-4	64.2	87.8	90.0	96.1
R-5/6	R-4	R-5/6	64.4	88.1	90.1	95.7
R-4	R-5/6	R-5/6	64.2	87.9	89.7	95.5
R-5/6	R-5/6	R-5/6	64.7	88.5	90.5	96.4

Table I: Comparison (\uparrow Acc. %) between RWKV-4 (R-4) and RWKV-5/6 (R-5/6).

A.2 Study on Learnable Weights

In our design of CSM and TRM, learnable weights serve as significant roles in highlighting subjects from background and reconstructing disappearing temporal relation. From the results revealed in Table II, we observe that lw^Δ and lw° can both improve the performance of wide-angle FSAR. The absence of lw^Δ harms the adaptive subjects highlighting while the deficiency of lw° damages the bidirectional scanning. Therefore, we devise CSM and TRM both equipped with learnable weights.

lw^Δ	lw°	SSv2		Kinetics	
		1-shot	5-shot	1-shot	5-shot
\times	\times	61.8	85.2	85.7	91.1
\checkmark	\times	63.8	87.9	89.7	95.8
\times	\checkmark	62.1	86.6	89.4	95.1
\checkmark	\checkmark	64.7	88.5	90.5	96.4

Table II: Comparison (\uparrow Acc. %) of learnable weights.

Loss Design In the loss design, we fix \mathcal{L}_{ce} as the primary loss for classification and reveal experiments in Table III. As auxiliary loss, both \mathcal{L}_p^1 and \mathcal{L}_p^2 combined with \mathcal{L}_{ce} can improve the performance via further distinguishing similar classes of prototype. The simultaneous use of the three losses can obtain the best performance of wide-angle FSAR. Therefore, \mathcal{L}_{ce} , \mathcal{L}_p^1 , and \mathcal{L}_p^2 are necessary in Otter.

\mathcal{L}_{ce}	\mathcal{L}_p^1	\mathcal{L}_p^2	SSv2		Kinetics	
			1-shot	5-shot	1-shot	5-shot
	\checkmark	\times	63.3	84.8	89.8	95.5
\checkmark	\times	\checkmark	63.4	88.0	90.1	95.7
	\checkmark	\checkmark	64.7	88.5	90.5	96.4

Table III: Comparison (\uparrow Acc. %) of loss design.

A.3 Study on Loss Weight Factors

The training objective is the combination of \mathcal{L}_{ce} , \mathcal{L}_p^1 , and \mathcal{L}_p^2 with loss weight factors λ . Experiments are conducted and the results are illustrated in Table IV. As a role primarily used for classification, λ_0 for \mathcal{L}_{ce} should not be less than 0.5. Considering the similar function of \mathcal{L}_p^1 and \mathcal{L}_p^2 , λ_1 and λ_2 should be equal. The performance is improved with the increasing λ_0 but begins to decline when $\lambda_0 > 0.8$. The above results confirm the loss weight factors.

λ_0	λ_1	λ_2	SSv2		Kinetics	
			1-shot	5-shot	1-shot	5-shot
0.50	0.25	0.25	62.9	87.6	89.6	95.6
0.60	0.20	0.20	64.1	88.0	89.9	95.9
0.70	0.15	0.15	64.3	88.2	90.3	96.2
0.80	0.10	0.10	64.7	88.5	90.5	96.4
0.90	0.05	0.05	64.4	88.4	90.2	96.2

Table IV: Comparison (\uparrow Acc. %) of loss factors.

A.4 Study on Various Types of Prototype

There are three types of prototype construction including attention-based calculation $\text{Attn}(\cdot)$ (Wang et al. 2022), query-specific prototype $\text{Q-Sp}(\cdot)$ (Perrett et al. 2021), and averaging calculation $\text{Avg}(\cdot)$ (Huang et al. 2025). Experiments about compatibility of Otter and prototype construction is conducted in Table V. Although $\text{Attn}(\cdot)$ and $\text{Q-Sp}(\cdot)$ with extra calculation achieve advanced performance in their work, the fitness with our Otter is not the best. Therefore, we select simple $\text{Avg}(\cdot)$ as our prototype.

Prototype	SSv2		Kinetics	
	1-shot	5-shot	1-shot	5-shot
$\text{Attn}(\cdot)$	63.9	87.1	89.3	94.9
$\text{Q-Sp}(\cdot)$	64.5	88.5	90.1	96.0
$\text{Avg}(\cdot)$	64.7	88.5	90.5	96.4

Table V: Comparison (\uparrow Acc. %) of various prototype types.

B Additional Wide-Angle Evaluation

B.1 Details of Wider FoV Simulation

From previous definition (Liao et al. 2023), FoV is only determined by camera CMOS size ($H_c \times W_c$) and lens focal length (L_f). Related calculation is written as

$$FoV = 2\arctan\left(\frac{\Delta}{2L_f}\right), \forall \Delta \in (H_c, W_c). \quad (I)$$

Image size is positively correlated with the CMOS size, while the distortion is negatively correlated with the focal length (Hu et al. 2022). Therefore, directly applying larger outpainting magnification (U_m) and introducing larger distortion factor (U_d) can simulate wider FoV. A group of simulation with five various levels is provided in Figure I. We observe that a wider FoV means more background. Meanwhile, distortion is more exaggerated. Wide-angle datasets always correct them for stable training. Re-adding distortion makes wide-angle FSAR more challenging.



Figure I: Examples with various wide FoV levels. To be specific, each level is a combination of U_m and U_d .

B.2 Temporal Relation

According to OTAM (Cao et al. 2020), DTW scores calculated from two sequences (\downarrow lower indicates better) can reflect the quality of temporal relation via alignment degree. The curves are shown in Figure II. We observe that models equipped with Otter converge much faster than those without Otter under any few-shot setting. The convergence points for the 5-shot are much earlier due to the increased number of training samples. Under the 1-shot setting of FSAR, the DTW curves without Otter even do not converge under Lv.1 or 2 FoV, indicating a more time-consuming training. Therefore, it is evident that Otter can effectively reconstruct temporal relations of wide-angle FSAR.

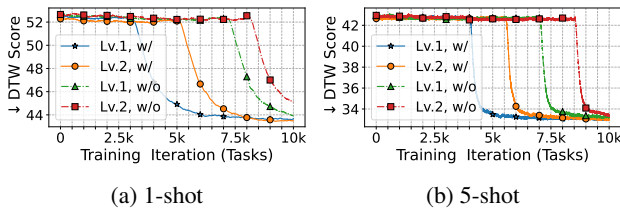


Figure II: \downarrow DTW scores under 1-shot setting during training on VideoBadminton. In specific, “Lv.1, w/” denotes model equipped with Otter and samples with Lv.1 FoV.

B.3 T-SNE Visualization

From the t-SNE (Van der Maaten and Hinton 2008) revealed in Figure III, the wide-angle actions are hard to be separated and clustered well without any assistance. Samples with Lv.4 FoV simulation are scattered everywhere. The above observation prove the difficulties in wide-angle FSAR. On the contrary, Otter clusters samples from same class and scatters others better. Although these special samples with 100% expanding magnification are located at the edge of each class, the cluster condition of them is much better.

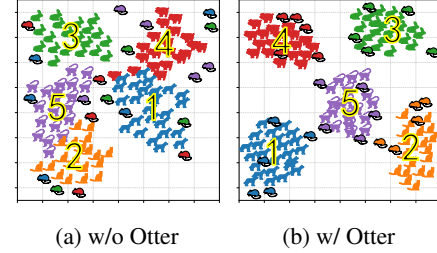


Figure III: T-SNE visualization of five action classes in support from Kinetics (25-shot). Blue: “ice skating”, Orange: “snowboarding”, Green: “paragliding”, Red: “skateboarding”, Purple: “crossing river”. Dots with black borders are samples with Lv.4 FoV simulation.

B.4 Additional CAM Visualization

Additional CAM visualization for wide-angle samples are provided in Figure IV. Taking “crossing river” as an example, it is evident that the model without Otter focuses on “forests” due to their larger proportion in the frames. Although subject “Jeep” is included, recognition is inevitably interfered with by the background. In contrast, Otter accurately highlights the subject while not completely ignoring the background, thereby achieving better performance. This focus pattern is consistent across the other two examples. These CAM visualization demonstrate that Otter mitigates background distractions, helping models better understand challenging actions in wide-angle scenario.

C Robustness Study

In order to explore robustness of Otter, we select two groups of noise added into $\mathcal{D}_{\text{test}}$ of FSAR. The first group is task-based including sample-level and frame-level noise for simulating unexpected circumstances during data collection. As revealed in Figure V, another group is visual noise such as zoom, Gaussian, rainy, and light noise, for simulating different shooting situations. Specifically, zoom frames are imposed by variation in optimal zoom while Gaussian noise is related to digital issues of hardware. Changeable weather and lighting conditions result in rainy and light noise.

C.1 Sample-Level Noise

Wide-angle samples from other classes may be mixed into a particular class. Correcting sample-level noise is time-consuming and laborious. Therefore, directly testing wide-angle FSAR on sample-level noise can reflect the robustness

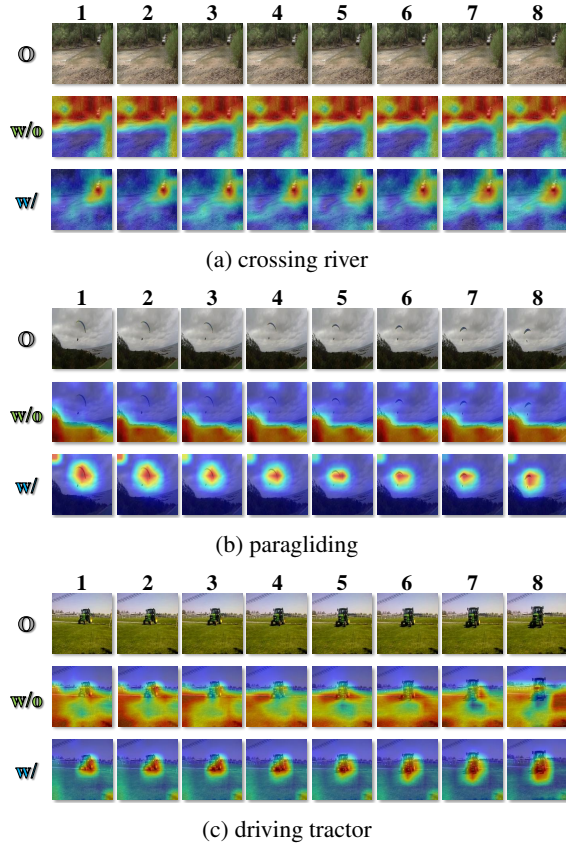


Figure IV: Additional CAM of “crossing river”, “paragliding”, and “driving tractor” from Kinetics dataset.

of a method. The experimental results are indicated in Table VI. It is obvious that the introduce of sample-level has negative impacts on the performance of wide-angle FSAR. The results decline with the increasing ratio of sample-level noise. However, we find that the robustness of our proposed Otter is better than other recent methods.

Datasets	Methods	Sample-Level Noise Ratio				
		0%	10%	20%	30%	40%
SSv2	MoLo	72.5	70.5	68.2	66.4	64.1
	SOAP	87.3	85.1	83.0	80.8	78.7
	Manta	89.6	87.6	86.2	83.1	80.9
	Otter	90.2	89.4	88.2	86.6	85.5
Kinetics	MoLo	87.5	85.1	83.4	80.8	78.1
	SOAP	95.9	94.2	92.1	89.7	87.5
	Manta	96.1	94.2	91.9	90.1	87.8
	Otter	98.4	97.5	96.2	95.0	93.8

Table VI: Comparison (\uparrow Acc. %) with sample-level noise under 5-way 10-shot setting.

C.2 Frame-Level Noise

Multiple irrelevant frames mixed into wide-angle samples are called as frame-level noise. Serving as a unexpected situation of data collection, robustness of methods can also be

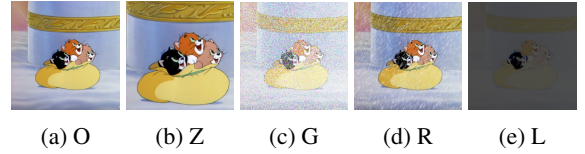


Figure V: Different kinds of noise. In specific, O, Z, G, R, and L denote original frames, zoom, Gaussian, rainy, and light noise, respectively.

reflected by frame-level noise. From the results in Table VII, we observe that the performance of wide-angle FSAR is harmed with the increasing number of noisy frames. The reason for this phenomenon is that frame-level noise further disorganizes subjects and temporal relation. Under the circumstance, our Otter still reveals stable performance, reflecting better robustness of frame-level noise.

Datasets	Methods	Noisy Frame Numbers				
		0	1	2	3	4
SSv2	MoLo	72.5	69.3	66.5	63.3	59.6
	SOAP	87.3	84.1	80.9	78.0	75.6
	Manta	89.6	86.4	83.2	80.4	77.3
	Otter	90.2	89.0	88.2	87.2	86.0
Kinetics	MoLo	87.5	84.3	81.5	78.0	75.3
	SOAP	95.9	93.1	90.2	87.6	84.1
	Manta	96.1	93.0	89.7	86.8	83.7
	Otter	98.4	97.1	95.7	94.5	93.2

Table VII: Comparison (\uparrow Acc. %) with frame-level noise under 5-way 10-shot setting.

C.3 Visual-Based Noise

Visual-based noise challenges the robustness of a method. Therefore, we add each type of visual-based noise to 25% samples for creating more complex wide-angle FSAR tasks. As shown in Table VIII, the zoom noise has the largest negative impact on the performance. Other types of visual-based noise more or less harm the results. However, we observe that our Otter can keep the SOTA performance under those challenging environment. These phenomena in wide-angle FSAR reflect the better robustness of the proposed Otter.

Datasets	Methods	Visual-Based Noise Type				
		O	Z	G	R	L
SSv2	MoLo	72.5	70.0	70.3	69.7	69.8
	SOAP	87.3	84.7	84.0	84.6	86.1
	Manta	89.6	87.5	88.7	88.8	87.4
	Otter	90.2	89.6	89.6	89.3	89.0
Kinetics	MoLo	87.5	85.2	86.3	86.7	85.9
	SOAP	95.9	93.6	94	94.4	93.9
	Manta	96.1	93.9	95.0	95.1	94.8
	Otter	98.4	97.9	98.0	97.7	97.8

Table VIII: Comparison (\uparrow Acc. %) with various types of 25% visual-based noise under 5-way 10-shot setting.

C.4 Cross Dataset Testing

In real-world scenario, various data distributions exist. Therefore, we apply the cross dataset method (training and testing on various datasets) for the simulation of different data distributions. SSv2 and Kinetics with three non-overlapping sets are utilized. Then overlapping classes of $\mathcal{D}_{\text{train}}$ and $\mathcal{D}_{\text{test}}$ from different datasets are further removed. From the results revealed in Table IX, despite cross-dataset setting degrading the performance, Otter can keep ahead of other methods. This trend similar with the regular test setting highlights the robustness of Otter.

Methods	KI→SS (SS→SS)		SS→KI (KI→KI)	
	1-shot	5-shot	1-shot	5-shot
MoLo	53.7 (56.6)	68.7 (70.7)	71.5 (74.2)	83.2 (85.7)
SOAP	60.0 (61.9)	84.5 (85.8)	84.1 (86.1)	91.1 (93.8)
Manta	61.5 (63.4)	86.4 (87.4)	86.3 (87.4)	91.8 (94.2)
Otter	63.1 (64.7)	86.7 (88.5)	89.2 (90.5)	94.0 (96.4)

Table IX: Comparison (\uparrow Acc. %) with cross dataset (large fonts) and regular testing (small fonts in brackets). KI→SS: Kinetics training while SSv2 testing, SS→KI: SSv2 training while Kinetics testing, SS→SS: training and testing both on SSv2, KI→KI: training and testing both on Kinetics.

C.5 Any-Shot Testing

In real-world application, ensuring shot number of each class equal is challenging. In order to create a more authentic testing environment for robustness, we apply the any-shot setup ($1 \leq K \leq 5$). From the results demonstrated in Table X, we observe that the performance of Otter defeats other methods, reflecting our Otter has a better robustness for applications in real-world scenario.

Methods	SSv2	Kinetics
MoLo	64.6 \pm 1.5	80.2 \pm 1.8
SOAP	73.8 \pm 1.4	89.1 \pm 1.3
Manta	75.2 \pm 1.1	90.6 \pm 1.3
Otter	77.4 \pm 0.6	93.6 \pm 0.7

Table X: Comparison (\uparrow Acc. %) with 95% confidence interval of 5-way any-shot setting.

D Computational Complexity

D.1 Inference Speed

To evaluate the model under practical conditions with limited resources, we conducted 10,000 tasks using a single 24GB NVIDIA GeForce RTX 3090 GPU on a server. From results demonstrated in Table XI, we find that the inference speed of MoLo and SOAP is slow because of Transformer with high computational complexity. On the contrary, Mamba-based Manta and RWKV-based Otter is much faster than previous Transformer-based methods. Considering the accuracy of classification, the proposed Otter is more suitable for practical applications.

Methods	SSv2		Kinetics	
	1-shot	5-shot	1-shot	5-shot
MoLo	7.83	8.02	7.64	8.14
SOAP	7.44	7.86	7.21	7.72
Manta	4.25	4.61	4.42	4.56
Otter	4.13	4.24	4.35	4.48

Table XI: Inference speed (\downarrow hour) with 10,000 random tasks on single 24GB NVIDIA GeForce RTX 3090 GPU.

D.2 Major Tensor Changes

The tensor changes detailed in Table XII offer deeper insights into Otter. For simplicity, we use the wildcard symbol Δ as in the main paper. These tensor changes facilitate the determination of hyper-parameters, such as the patch size ($p = 56$). Additionally, we observe that the primary computational burden lies in the Seg(\cdot, \cdot) and RT(\dots, \cdot, \dots) components of the CSM, confirming the single-scale patch design for reducing computational cost. In the following pseudo-code, we provide the further analysis of computational complexity in the proposed Otter.

Operation	Input	Input Size	Output	Output Size
Seg	Δ	$[F, C, H, W]$	Δ^p	$[F, C, p, p]$
RT	$lw^\Delta \odot \Delta^\beta$	$[F, C, p, p]$	Δ	$[F, C, H, W]$
CSM	$S^{c,k}, Q^\gamma$	$[F, C, H, W]$	$\hat{S}^{c,k}, \hat{Q}^\gamma$	$[F, C, H, W]$
f_θ	$\hat{S}^{c,k}, \hat{Q}^\gamma$	$[F, C, H, W]$	$S_f^{c,k}, Q_f^\gamma$	$[F, D]$
TRM	$lw^\Delta \odot \Delta$	$[F, D]$	Δ	$[F, D]$

Table XII: Major tensor changes in the proposed Otter. Wildcard symbol Δ is applied for simple demonstration and notions are consistent with the main paper.

D.3 Pseudo-Code

The primary computational burden lies in the Compound Segmentation Module (CSM). For complexity analysis, the related pseudo-code is listed in Algorithm 1. Considering the low computational complexity of core units including S-Mix(\cdot), T-Mix(\cdot), and C-Mix(\cdot) in RWKV, the functions Seg(\cdot, \cdot) and RT(\dots, \cdot, \dots) form the main structure with nested loops. Both the inner and outer loops have a computational complexity of $O(p)$. Consequently, the total complexity of the CSM is $O(p^2)$. Given the determined size and single-scale design of p ($p = 56$), the additional computational burden introduced by Otter is negligible, ensuring its usability in real-world applications.

E Contribution Statement

This work represents a **collaborative effort** among all authors, each contributing expertise from different perspectives. The specific contributions are as follows:

- **Wenbo Huang (Southeast University, China; Institute of Science Tokyo, Japan):** Firstly proposing the idea of applying RWKV in FSAR, implementing all code of Otter, designing wide-angle evaluation in § B, conducting all experiments, deriving all mathematical formulas, all

Algorithm 1: Compound Motion Segmentation

Input: $\Delta \in \mathbb{R}^{F \times C \times H \times W}$, $\forall \Delta \in \{S^{c,k}, Q^\gamma\}$,
 $NP \ (H \mid NP, W \mid NP, NP \in \mathbb{Z}^+)$.
Output: $\hat{\Delta} \in \mathbb{R}^{F \times C \times H \times W}$, $\forall \Delta \in \{S^{c,k}, Q^\gamma\}$.

```
1  $\hat{\Delta}_1 \leftarrow \emptyset$ ;  
2 if  $H \% NP == 0 \ \& \ W \% NP == 0$  then  
3    $Block \leftarrow (H/NP, W/NP)$ ;  
4   if  $Block[0] == Block[1]$  then  
5      $p_H \leftarrow Block[0]$ ;  
6      $p_W \leftarrow Block[1]$ ;  
7     for each  $i \in [0, p_H]$  do  
8       for each  $j \in [0, p_W]$  do  
9         /* Seg ( $\cdot, \cdot$ ) Start */  
10         $s \leftarrow [i \times p_H, j \times p_W]$ ;  
11         $e \leftarrow [(i+1) \times p_H, (j+1) \times p_W]$ ;  
12         $p \leftarrow \Delta[:, :, s(0) : e(0), s(1) : e(1)]$ ;  
13         $p1 \leftarrow S-Mix(p) \oplus p$ ;  
14         $p2 \leftarrow C-Mix(p1) \oplus p1$ ;  
15         $lw \leftarrow \sigma[Conv(p2) \oplus p]$ ;  
16         $\hat{p} \leftarrow lw \odot p2$ ;  
17        /* Seg ( $\cdot, \cdot$ ) End */  
18        /* RT ( $\dots, \dots$ ) Start */  
19         $\hat{\Delta}_1[:, :, s(0) : e(0), s(1) : e(1)] \leftarrow \hat{p}$ ;  
20        /* RT ( $\dots, \dots$ ) End */  
21      end  
22    end  
23   $\hat{\Delta}_2 \leftarrow S-Mix(\hat{\Delta}_1) \oplus \hat{\Delta}_1$ ;  
24   $\hat{\Delta} \leftarrow C-Mix(\hat{\Delta}_2) \oplus \hat{\Delta}_2$ ;  
25 end  
26 return  $\hat{\Delta}$ 
```

data collection, all figure drawing, all table organizing, and completing original manuscript.

- **Jinghui Zhang (Southeast University, China):** Providing experimental platform in China, supervision in China, writing polish mainly on logic of introduction, checking results, and funding acquisition.
- **Zhenghao Chen (The University of Newcastle, Australia):** Writing polish mainly on authentic expression, clarifying the definition of wide-angle, amending mathematical formulas, checking experimental results, rebuttal assistance, and funding acquisition.
- **Guang Li (Hokkaido University, Japan):** Refining Idea of Otter, writing polish mainly on descriptions of results, rebuttal assistance, and funding acquisition.
- **Lei Zhang (Nanjing Normal University, China):** Proposing the extra experiments on real wide-angle dataset VideoBadminton, guiding CAM visualization, rebuttal assistance, and funding acquisition.
- **Yang Cao (Institute of Science Tokyo, Japan):** Verification of the overall structure, providing experimental platform in Japan, supervision in Japan, rebuttal assistance, and funding acquisition.
- **Fang Dong (Southeast University, China):** Funding acquisition.

- **Takahiro Ogawa (Hokkaido University, Japan):** Writing polish mainly on numerous details, guiding t-SNE visualization, rebuttal assistance, and funding acquisition.
- **Miki Haseyama (Hokkaido University, Japan):** Funding acquisition.

Acknowledgments

The authors would like to appreciate all participants of peer review and cloud servers provided by Paratera Ltd. Wenbo Huang sincerely thanks those who offered companionship and encouragement during the most challenging times, even though life has since taken everyone on different paths. This work is supported by Frontier Technologies Research and Development Program of Jiangsu under Grant No. BF2024070; National Natural Science Foundation of China under Grants Nos. 62472094, 62072099, 62232004, 62373194, 62276063; Jiangsu Provincial Key Laboratory of Network and Information Security under Grant No. BM2003201; Key Laboratory of Computer Network and Information Integration (Ministry of Education, China) under Grant No. 93K-9; the Fundamental Research Funds for the Central Universities; JSPS KAKENHI Nos. JP23K21676, JP24K02942, JP24K23849, JP25K21218, JP23K24851; JST PRESTO Grant No. JPMJPR23P5; JST CREST Grant No. JPMJCR21M2; JST NEXUS Grant No. JPMJNX25C4; and Startup Funds from The University of Newcastle, Australia.

References

- Cao, K.; Ji, J.; Cao, Z.; Chang, C.-Y.; and Niebles, J. C. 2020. Few-shot video classification via temporal alignment. In *CVPR*.
- Carreira, J.; and Zisserman, A. 2017. Quo vadis, action recognition? a new model and the kinetics dataset. In *CVPR*.
- Chen, Z.; Fu, Y.; Wang, Y.-X.; Ma, L.; Liu, W.; and Hebert, M. 2019. Image deformation meta-networks for one-shot learning. In *CVPR*.
- Duan, Y.; Wang, W.; Chen, Z.; Zhu, X.; Lu, L.; Lu, T.; Qiao, Y.; Li, H.; Dai, J.; and Wang, W. 2024. Vision-rwkv: Efficient and scalable visual perception with rwkv-like architectures. *arXiv preprint arXiv:2403.02308*.
- Fei, Z.; Fan, M.; Yu, C.; Li, D.; and Huang, J. 2024. Diffusion-rwkv: Scaling rwkv-like architectures for diffusion models. *arXiv preprint arXiv:2404.04478*.
- Fei-Fei, L.; Fergus, R.; and Perona, P. 2006. One-shot learning of object categories. *IEEE Transactions on Pattern Analysis and Machine Intelligence*.
- Finn, C.; Abbeel, P.; and Levine, S. 2017. Model-agnostic meta-learning for fast adaptation of deep networks. In *ICML*.
- Fu, Y.; Zhang, L.; Wang, J.; Fu, Y.; and Jiang, Y.-G. 2020. Depth guided adaptive meta-fusion network for few-shot video recognition. In *ACM MM*.
- Goyal, R.; Ebrahimi Kahou, S.; Michalski, V.; Materzynska, J.; Westphal, S.; Kim, H.; Haenel, V.; Fruend, I.; Yianilos, P.; Mueller-Freitag, M.; et al. 2017. The” something

- something” video database for learning and evaluating visual common sense. In *ICCV*.
- Gu, T.; Yang, K.; An, X.; Feng, Z.; Liu, D.; Cai, W.; and Deng, J. 2024. RWKV-CLIP: A Robust Vision-Language Representation Learner. *arXiv preprint arXiv:2406.06973*.
- Hao, F.; He, F.; Cheng, J.; Wang, L.; Cao, J.; and Tao, D. 2019. Collect and select: Semantic alignment metric learning for few-shot learning. In *CVPR*.
- Hariharan, B.; and Girshick, R. 2017. Low-shot visual recognition by shrinking and hallucinating features. In *ICCV*.
- He, Q.; Zhang, J.; Peng, J.; He, H.; Li, X.; Wang, Y.; and Wang, C. 2024. Pointtrwkv: Efficient rwkv-like model for hierarchical point cloud learning. *arXiv preprint arXiv:2405.15214*.
- Hold-Geoffroy, Y.; Piché-Meunier, D.; Sunkavalli, K.; Bazin, J.-C.; Rameau, F.; and Lalonde, J.-F. 2023. A perceptual measure for deep single image camera and lens calibration. *IEEE Transactions on Pattern Analysis and Machine Intelligence*.
- Hu, Z.-Y.; Zhang, Y.-L.; Pan, C.; Dou, J.-Y.; Li, Z.-Z.; Tian, Z.-N.; Mao, J.-W.; Chen, Q.-D.; and Sun, H.-B. 2022. Miniature optoelectronic compound eye camera. *Nature Communications*.
- Huang, W.; Zhang, J.; Li, G.; Zhang, L.; Wang, S.; Dong, F.; Jin, J.; Ogawa, T.; and Haseyama, M. 2025. Manta: Enhancing Mamba for Few-Shot Action Recognition of Long Sub-Sequence. In *AAAI*.
- Huang, W.; Zhang, J.; Qian, X.; Wu, Z.; Wang, M.; and Zhang, L. 2024. SOAP: Enhancing Spatio-Temporal Relation and Motion Information Capturing for Few-Shot Action Recognition. In *ACM MM*.
- Jamal, M. A.; and Qi, G.-J. 2019. Task agnostic meta-learning for few-shot learning. In *CVPR*.
- Kay, W.; Carreira, J.; Simonyan, K.; Zhang, B.; Hillier, C.; Vijayanarasimhan, S.; Viola, F.; Green, T.; Back, T.; Natsev, P.; et al. 2017. The kinetics human action video dataset. *arXiv preprint arXiv:1705.06950*.
- Kuehne, H.; Jhuang, H.; Garrote, E.; Poggio, T.; and Serre, T. 2011. HMDB: a large video database for human motion recognition. In *ICCV*.
- Lai, W.-S.; Shih, Y.; Liang, C.-K.; and Yang, M.-H. 2021. Correcting face distortion in wide-angle videos. *IEEE Transactions on Image Processing*.
- Lee, J.; Go, H.; Lee, H.; Cho, S.; Sung, M.; and Kim, J. 2021. Ctrl-c: Camera calibration transformer with line-classification. In *ICCV*.
- Li, K.; Zhang, Y.; Li, K.; and Fu, Y. 2020. Adversarial feature hallucination networks for few-shot learning. In *CVPR*.
- Li, Q.; Chiu, T.-C.; Huang, H.-W.; Sun, M.-T.; and Ku, W.-S. 2024. Benchmarking Badminton Action Recognition with a New Fine-Grained Dataset. *arXiv preprint arXiv:2403.12385*.
- Li, S.; Liu, H.; Qian, R.; Li, Y.; See, J.; Fei, M.; Yu, X.; and Lin, W. 2022. Ta2n: Two-stage action alignment network for few-shot action recognition. In *AAAI*.
- Liao, K.; Nie, L.; Huang, S.; Lin, C.; Zhang, J.; Zhao, Y.; Gabbouj, M.; and Tao, D. 2023. Deep learning for camera calibration and beyond: A survey. *arXiv preprint arXiv:2303.10559*.
- Liu, B.; Zheng, T.; Zheng, P.; Liu, D.; Qu, X.; Gao, J.; Dong, J.; and Wang, X. 2023. Lite-MKD: A Multi-modal Knowledge Distillation Framework for Lightweight Few-shot Action Recognition. In *ACM MM*.
- Oreshkin, B.; Rodríguez López, P.; and Lacoste, A. 2018. Tadam: Task dependent adaptive metric for improved few-shot learning. In *NeurIPS*.
- Peng, B.; Alcaide, E.; Anthony, Q.; Albalak, A.; Arcadinho, S.; Biderman, S.; Cao, H.; Cheng, X.; Chung, M.; Grella, M.; et al. 2023. Rwkv: Reinventing rnns for the transformer era. In *EMNLP*.
- Peng, B.; Goldstein, D.; Anthony, Q.; Albalak, A.; Alcaide, E.; Biderman, S.; Cheah, E.; Du, X.; Ferdinan, T.; Hou, H.; et al. 2024. Eagle and finch: Rwkv with matrix-valued states and dynamic recurrence. In *COLM*.
- Perrett, T.; Masullo, A.; Burghardt, T.; Mirmehdi, M.; and Damen, D. 2021. Temporal-relational crosstransformers for few-shot action recognition. In *CVPR*.
- Rajeswaran, A.; Finn, C.; Kakade, S. M.; and Levine, S. 2019. Meta-learning with implicit gradients. In *NeurIPS*.
- Ravi, S.; and Larochelle, H. 2017. Optimization as a model for few-shot learning. In *ICLR*.
- Rusu, A. A.; Rao, D.; Sygnowski, J.; Vinyals, O.; Pascanu, R.; Osindero, S.; and Hadsell, R. 2018. Meta-learning with latent embedding optimization. In *ICLR*.
- Snell, J.; Swersky, K.; and Zemel, R. 2017. Prototypical networks for few-shot learning. In *NeurIPS*.
- Sung, F.; Yang, Y.; Zhang, L.; Xiang, T.; Torr, P. H.; and Hospedales, T. M. 2018. Learning to compare: Relation network for few-shot learning. In *CVPR*.
- Thatipelli, A.; Narayan, S.; Khan, S.; Anwer, R. M.; Khan, F. S.; and Ghanem, B. 2022. Spatio-temporal relation modeling for few-shot action recognition. In *CVPR*.
- Van der Maaten, L.; and Hinton, G. 2008. Visualizing data using t-SNE. *Journal of machine learning research*.
- Wang, L.; Xiong, Y.; Wang, Z.; Qiao, Y.; Lin, D.; Tang, X.; and Van Gool, L. 2016. Temporal segment networks: Towards good practices for deep action recognition. In *ECCV*.
- Wang, X.; Zhang, S.; Qing, Z.; Gao, C.; Zhang, Y.; Zhao, D.; and Sang, N. 2023a. MoLo: Motion-augmented Long-short Contrastive Learning for Few-shot Action Recognition. In *CVPR*.
- Wang, X.; Zhang, S.; Qing, Z.; Tang, M.; Zuo, Z.; Gao, C.; Jin, R.; and Sang, N. 2022. Hybrid relation guided set matching for few-shot action recognition. In *CVPR*.
- Wang, X.; Zhu, Z.; Xu, W.; Zhang, Y.; Wei, Y.; Chi, X.; Ye, Y.; Du, D.; Lu, J.; and Wang, X. 2023b. Openoccupancy: A large scale benchmark for surrounding semantic occupancy perception. In *ICCV*.
- Wang, Y.-X.; Girshick, R.; Hebert, M.; and Hariharan, B. 2018. Low-shot learning from imaginary data. In *CVPR*.

Wang, Z.; Zhao, Y.; Li, J.; and Tian, Y. 2020. Cooperative bi-path metric for few-shot learning. In *ACM MM*.

Wanyan, Y.; Yang, X.; Chen, C.; and Xu, C. 2023. Active Exploration of Multimodal Complementarity for Few-Shot Action Recognition. In *CVPR*.

Wu, J.; Zhang, T.; Zhang, Z.; Wu, F.; and Zhang, Y. 2022. Motion-modulated temporal fragment alignment network for few-shot action recognition. In *CVPR*.

Xing, J.; Wang, M.; Liu, Y.; and Mu, B. 2023a. Revisiting the Spatial and Temporal Modeling for Few-shot Action Recognition. In *AAAI*.

Xing, J.; Wang, M.; Ruan, Y.; Chen, B.; Guo, Y.; Mu, B.; Dai, G.; Wang, J.; and Liu, Y. 2023b. Boosting Few-shot Action Recognition with Graph-guided Hybrid Matching. In *ICCV*.

Yan, C.; Zhang, S.; Liu, Y.; Pang, G.; and Wang, W. 2023. Feature prediction diffusion model for video anomaly detection. In *ICCV*.

Yu, T.; Chen, P.; Dang, Y.; Huan, R.; and Liang, R. 2023. Multi-Speed Global Contextual Subspace Matching for Few-Shot Action Recognition. In *ACM MM*.

Yuan, H.; Li, X.; Qi, L.; Zhang, T.; Yang, M.-H.; Yan, S.; and Loy, C. C. 2024. Mamba or rwkv: Exploring high-quality and high-efficiency segment anything model. *arXiv preprint arXiv:2406.19369*.

Zhang, H.; Zhang, L.; Qi, X.; Li, H.; Torr, P. H.; and Koniusz, P. 2020. Few-shot action recognition with permutation-invariant attention. In *ECCV*.

Zhang, K.; Huang, J.-B.; Echevarria, J.; DiVerdi, S.; and Hertzmann, A. 2025. MaDCoW: Marginal Distortion Correction for Wide-Angle Photography with Arbitrary Objects. In *CVPR*.

Zhang, R.; Che, T.; Ghahramani, Z.; Bengio, Y.; and Song, Y. 2018. Metagan: An adversarial approach to few-shot learning. In *NeurIPS*.

Zhang, S.; Huang, J.; Zhou, Q.; Wang, Z.; Wang, F.; Luo, J.; and Yan, J. 2024. Continuous-multiple image outpainting in one-step via positional query and a diffusion-based approach. In *ICLR*.

Zhang, S.; Zhou, J.; and He, X. 2021. Learning implicit temporal alignment for few-shot video classification. In *IJCAI*.

Zhang, Y.; Fu, Y.; Ma, X.; Qi, L.; Chen, J.; Wu, Z.; and Jiang, Y.-G. 2023. On the Importance of Spatial Relations for Few-shot Action Recognition. In *ACM MM*.

Zhao, M.; Wang, M.; Bai, F.; Li, B.; Wang, J.; and Zhou, S. 2022. C3-stsr: Scene text image super-resolution with triple clues. In *IJCAI*.

Zhu, L.; and Yang, Y. 2018. Compound memory networks for few-shot video classification. In *ECCV*.